Article

Matrix-induced defects and molecular doping in the afterglow of SiO$_2$ microparticles

Xue Chen[1,2,3,4], Mengfen Che[1,2,3,4], Weidong Xu[1,2,3], Zhongbin Wu[1,2,3], Yung Doug Suh[5], Suli Wu[6], Xiaowang Liu[1,2,3,4] ✉ & Wei Huang[1,2,3,4,7,8] ✉

A deep understanding of how the host matrix influences the afterglow properties of molecule dopants is crucial for designing advanced afterglow materials. Despite its appeal, the impact of defects on the afterglow performance in molecule-doped SiO$_2$ matrices has remained largely unexplored. Herein, we detail the synthesis of monodisperse SiO$_2$ microparticles by hydrothermally doping molecules, such as 4-phenylpyridine, 4,4′-bipyridine, and 1,4-bis(pyrid-4-yl)benzene. Our results demonstrate that hydrothermal reactions induce not only the formation of emissive defects in the SiO$_2$ matrix but also enable molecule doping through SiO$_2$ pseudomorphic transformation. Optical analyses reveal a remarkable afterglow activation of doped molecules, driven by a synergistic interplay of hydrogen bonding and physical fixation. Specifically, 4-phenylpyridine doping leads to an impressive 227- and 271-fold enhancement in fluorescence and afterglow, respectively, and an extraordinary 3711-fold enhancement in the afterglow lifetime of the resulting SiO$_2$ MPs. We also document hybrid states involving molecule dopants and SiO$_2$ defects, explaining energy transfer from molecule dopants to defects in both singlet and triplet states. The robust achievement of molecule doping provides flexibility to tailor excitation-dependent afterglow attributes while preserving angle-dependent structural colors, facilitating the creation of diverse building blocks for multiscale optical platforms for afterglow modulation and information encoding.

Silicon dioxide (SiO$_2$) is one of the most abundant materials on earth and holds significant technological importance. It serves as the fundamental material for modern electronics, functioning as a cornerstone for the production of semiconductors and microelectronic devices[1–8]. SiO$_2$ is also known to exhibit defects within its otherwise perfect structure even produced by the thermal oxidation of silicon. These defects encompass oxygen and silicon vacancies, as well as their interstitial counterparts, including Si−Si and O−O bonds, along with

[1]Frontiers Science Center for Flexible Electronics (FSCFE) & Institute of Flexible Electronics (IFE), Northwestern Polytechnical University, Xi'an 710072 Shaanxi, China. [2]MIIT Key Laboratory of Flexible Electronics (KLoFE), Northwestern Polytechnical University, Xi'an 710072 Shaanxi, China. [3]Shaanxi Key Laboratory of Flexible Electronics & Xi'an Key Laboratory of Flexible Electronics, Northwestern Polytechnical University, Xi'an 710072 Shaanxi, China. [4]Xi'an Key Laboratory of Biomedical Materials & Engineering, Xi'an Institute of Flexible Electronics, Northwestern Polytechnical University, Xi'an 710072 Shaanxi, China. [5]Department of Chemistry and School of Energy and Chemical Engineering UNIST, Ulsan 44919, Republic of South Korea. [6]State Key Laboratory of Fine Chemicals, Dalian University of Technology, 2nd Linggong Road, Dalian 116024, China. [7]State Key Laboratory of Organic Electronics and Information Displays & Institute of Advanced Materials(IAM), Nanjing University of Posts & Telecommunications, 9 Wenyuan Road, Nanjing 210023, China. [8]Key Laboratory of Flexible Electronics (KLOFE), Institute of Advanced Materials (IAM), Nanjing Tech University (Nanjing Tech), 30 South Puzhu Road, Nanjing 211816, China. ✉e-mail: iamxwliu@nwpu.edu.cn; vc@nwpu.edu.cn

under-coordinated silicon and oxygen atoms[9–12]. Defect type and concentration are affected by other factors such as irradiation, mechanical stress, temperature fluctuations, and the introduction of impurities[13–16]. The optical absorption and emission in pure SiO_2 materials are typically attributed by the presence of defects[10–12,17]. Nevertheless, the luminescence of pure SiO_2 remains inconspicuous when exposed to low-energy irradiation, unless subjected to high-temperature calcination or introduced with a sensitizer activator.

Luminescent dopants embedded within a solid SiO_2 matrix are expected to exhibit strong interactions with neighboring emissive defects when their energy levels align effectively (Fig. 1a). Through the choice of doped species in the form of either molecules or metal ions, the resultant SiO_2 show the promise to exhibit afterglow as an outcome of the stabilization of the triplet states of the dopants by hydrogen bonding and physical fixation effects or due to the energy storage by the intrinsic defects[18–20]. A deep understanding of the energy interaction between dopants and host defects is crucial for the rational development of afterglow materials[21–23]. Furthermore, deliberate control of energy transfer between singlet and triplet states of these two species enables a dual-channel approach to customize the afterglow properties of the doped SiO_2 composites including glow color and lifetime for widespread applications, such as sensing[24,25] and anti-counterfeiting[26–29] (Fig. 1b). In addition, the UV absorption cross-section of bicyclic aromatic molecules is ~10^{-16} cm², which is about ten times stronger than that of the defects in the SiO_2 matrix[30,31]. This significant difference further highlight the benefits in the production of enhanced defect emissions through molecule-to-defect energy transfer. Despite its appeal, the incorporation of dopants and abundant emissive structural defects with strategically designed energy levels into a SiO_2 platform remains a formidable challenge.

Here, we show that hydrothermal treatment of SiO_2 microparticles (MPs) at high temperatures not only facilitates the generation of emissive defects within the matrix but also allows for molecular doping, including 4-phenylpyridine (4-PP), 4,4′-bipyridine (4,4-BP), and 1,4-bis(pyrid-4-yl)benzene (1,4-DPB) through their pseudomorphic transformation. Optical analyses reveal that the doped molecules exhibit significant afterglow activation, driven by the synergistic effects of hydrogen bonding and physical fixation. In particular, doping with 4-PP results in a remarkable 227-fold and 271-fold increase in fluorescence and afterglow, respectively, and an extraordinary 3711-fold enhancement in the afterglow lifetime of the resulting SiO_2 MPs. We also demonstrate the feasibility of hybrid states between molecular dopants and SiO_2 defects, which facilitate energy transfer from the molecular dopants to the defects in both singlet and triplet states. The successful achievement of molecular doping allows for the customization of excitation-dependent afterglow properties while maintaining angle-dependent structural colors, enabling the development of versatile building blocks for multiscale optical platforms geared towards afterglow modulation and information encoding.

Results

Doping 4-PP into defect-enriched SiO₂ MPs

We first examined the feasibility with abundant emissive defects for monodisperse SiO_2 MPs derived by the modified stöber methods[32]. We found that the as-prepared SiO_2 MPs show an average diameter of 359 nm (Supplementary Fig. 1a, b) and exhibit
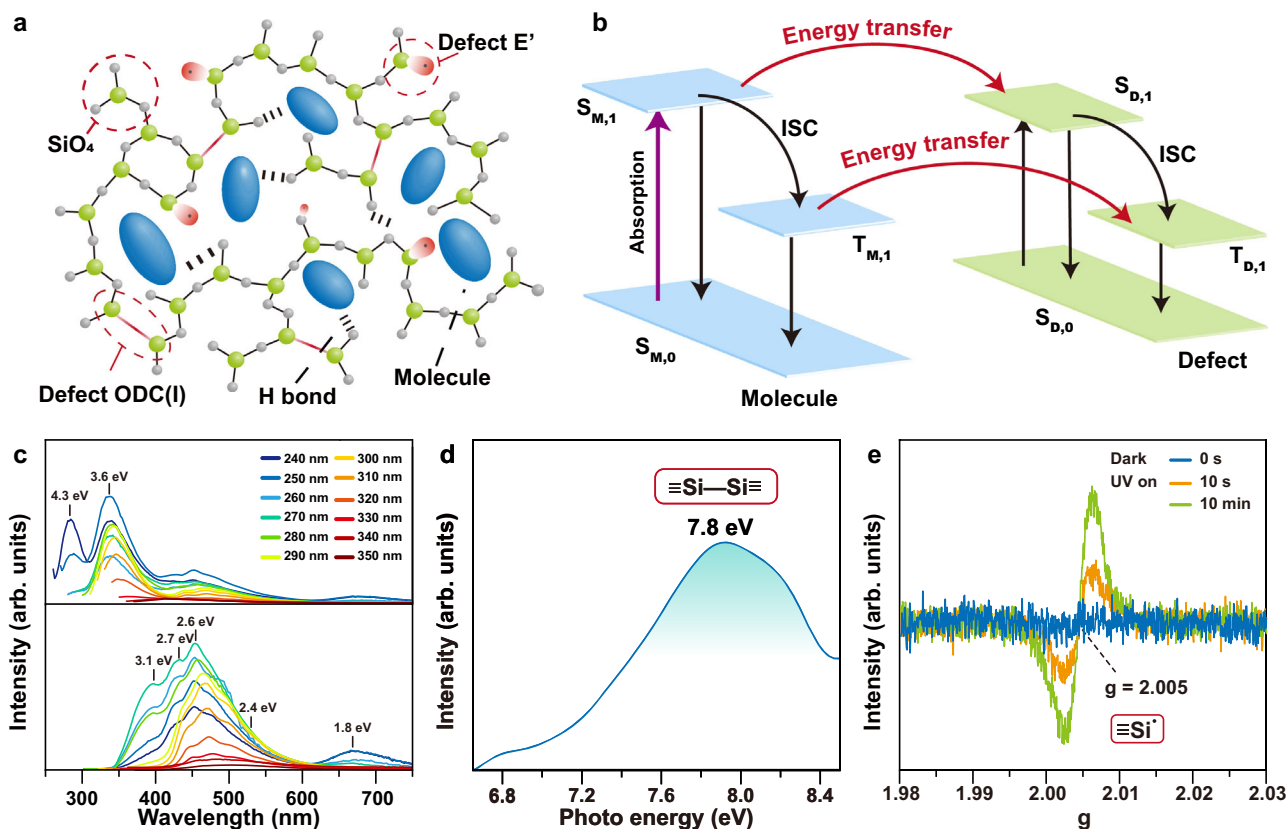

Fig. 1 | Interactions between molecule dopants and intrinsic defects in SiO₂ matrix. a Schematic depiction of the matrix structure of molecule-doped SiO_2. **b** Schematic illustration of energy transfer between molecule dopants and SiO_2 defects in both singlet and triplet states. **c** Short- (upper panel) and long-lived (lower panel) emission profiles of SiO_2 MPs under various excitation wavelengths at 77 K. The excitation wavelength was increased from 240 (navy) to 350 (darkred)

nm. The delay time was set at 2 ms for obtaining the long-lived emissions. It is noteworthy that SiO_2 MPs were prepared using a modified Stöber method, followed by hydrothermal treatment at 180 °C for 3 h. **d** Optical absorption band of the as-prepared SiO_2 MPs in the extreme UV spectral region. **e** ESR spectra of the as-prepared SiO_2 MPs measured under different conditions.

weak excitation-dependent emission profiles in the visible region (Supplementary Fig. 2a). More importantly, long-lived emissions were also observed under different excitation wavelengths (Supplementary Fig. 2b, c). The short- and long-lived emissions were attributed to the singlet and triplet state emissions for the defects in the SiO$_2$ MPs. Note that after being treated under hydrothermal conditions at 180 °C for 3 h, the excitation-dependent photoluminescence was retained (Supplementary Fig. 2d, e), and under excitation at 270 nm, the short-lived emission was found to main the same intensity with slight redshifts, while the long-lived emission was found to increase about 17.3 folds (Supplementary Fig. 2f). These results suggest that high-temperature hydrothermal treatment allows for improving matrix quality to suppress energy dissipation to enhance the phosphorescence by acceleration of redehydration reaction between neighboring hydroxyl groups.

Low-temperature luminescence spectroscopy showed the presence of unrelaxed oxygen-deficiency centers (ODCs) by the observation of fluorescence band at 284 nm (4.3 eV) upon excitation at 240–250 nm of the treated SiO$_2$ MPs (Fig. 1c). ODCs were confirmed by the observation of a long-lived emission at 466 nm (2.7 eV). Other defects, including non-bridging oxygen holes (1.8 eV), E'-like centers (2.2–2.4 eV), peroxy-radical hole trap (PRHT) (2.6 eV), dioxasilirane groups (3.1 eV), and oxygen excess defect (3.6 eV) were further confirmed by the emission profiles (Fig. 1c and Table S1). Note that the presence of relaxed ODC(I) was also confirmed by the appearance of an obvious absorption band at 7.8 eV at room temperature (Fig. 1d). The electron spin resonance (ESR) spectra suggest the feasibility of producing E' centers in the as-prepared SiO$_2$ MPs under stimulation of UV light (Fig. 1e), as evidenced by the observation of UV-triggered peaks with a g of 2.005. This is consistent with previous findings that kinds of paramagnetic defects can be generated upon UV irradiation[12]. Oxygen-deficient SiO$_2$ matrix shows a preference for E' centers, resulting from the photoinduced breaking of weak Si–Si bonds[33–35]. On a separate note, polysiloxanes typically exhibit a loose structure that allows for the formation of aggregated electron-rich clusters, leading to aggregation-induced emissions when terminal hydroxyl and carbonyl groups are introduced. However, they are unable to produce triplet-state emissions due to the ease of quenching by solvents and O$_2$[36,37]. Taken together, these results suggest that hydrothermally treated SiO$_2$ MPs contain abundant emissive defects with both singlet and triplet states, which are allowed to be utilized for energy transfer management with dopants to rational tuning of the combined afterglow properties.

We then conducted photophysical studies of our selected molecular dopants, including 4-tetraphenylpyridine (4-PP), 4,4′-bipyridine (4,4-BP), and 1,4-di(pyridin-4-yl)benzene (1,4-DPB) after doping them into a polyvinyl alcohol (PVA) matrix. The choice of PVA is due to its enriched –OH groups, which facilitate hydrogen bonding with molecular dopants, generating long-lived emissions of the doped molecules[38–41]. Our results indicate that the optimal excitation wavelengths are 250 nm for 4,4-BP, 312 nm for 4-PP, and 350 nm for 1,4-DPB. In addition, 4,4-BP exhibits phosphorescence at 430 nm; 4-PP exhibits fluorescence at 366 nm and phosphorescence at 455 nm; and 1,4-DPB exhibits fluorescence at 379 nm and phosphorescence at 517 nm (Supplementary Fig. 3). These findings demonstrate that phosphorescence bands progressively redshift from 4,4-BP and 4-PP and then to 1,4-DPB, establishing a foundation for studying energy transfer between doped molecules and defects at various energy levels.

In addition to enhancing the intrinsic afterglow emission, high-temperature hydrothermal reactions offer the opportunity to incorporate molecule dopants into SiO$_2$ MPs. Our findings reveal that subjecting a mixture of SiO$_2$ MPs and 4-PP to hydrothermal treatment at 180 °C for 3 h resulted in a slight reduction in the average diameter of 3 nm (Supplementary Fig. 4a), while preserving the monodisperse characteristics of the parent SiO$_2$ MPs (inset, Fig. 2a), as evidenced by

the observation of a single peak at 393 nm in the dynamic light scattering profile (Supplementary Fig. 4b). The success of 4-PP doping was supported by optical characterization of the resultant SiO$_2$ MPs. Upon UV excitation (310 nm), a bright blue emission was observed from an aqueous dispersion of the SiO$_2$ MPs, and the blue emission changed to cyan, which lasted more than 15 s when ceasing the excitation (Fig. 2b). When compared with undoped SiO$_2$ MPs, 4-PP-doped SiO$_2$ MPs showed a 227-fold enhancement in the fluorescence at 350 nm under the excitation (Upper panel, Fig. 2c), and the photoluminescence quantum yield was found to increase from near 0 to 17.88%. A delayed spectrum suggests the cyan emission at 472 nm, and the intensity was estimated to be about 271 times stronger than that of undoped SiO$_2$ MPs. Note that the lifetime of the cyan afterglow was estimated to be 3.60 s, 3711-fold longer than that of the defect emission for the undoped SiO$_2$ MPs. Temperature-dependent phosphorescence study showed a decline in the intensity with increasing the measurement temperatures, suggesting the nature of phosphorescence of the cyan afterglow for 4-PP dopants (Supplementary Fig. 5). On a separate note, ^{1}H nuclear magnetic resonance spectroscopy showed the integrity of the doped 4-PP molecules after the hydrothermal reaction, indicative of the doping of 4-PP molecules other than in situ generated carbon dots into the treated SiO$_2$ MPs (Supplementary Fig. 6a, b).

The pseudomorphic transformation of SiO$_2$ MPs facilitates the incorporation of 4-PP molecules into their matrix under hydrothermal conditions. Under hydrothermal conditions (Supplementary Fig. 7)[42], the SiO$_2$ matrix gradually dissolves in water, resulting in the formation of orthosilicic acid as the reaction temperature rises. Over prolonged reaction times, the dissolution and recondensation of orthosilicic acid on the surface of the etched SiO$_2$ MPs reach equilibrium. Upon the completion of the reaction, a substantial amount of orthosilicic acid residues persists in the reaction mixture, leading to a reduction in average size while maintaining a uniform size distribution. During the pseudomorphic transformation, the incorporation of 4-PP molecules into SiO$_2$ MPs is realized possibly with the assistance of the hydrogen bonding between the dopants and hydroxyl groups of SiO$_2$ matrix.

Optical characterization of 4-PP-doped SiO$_2$ MPs

Within the excitation wavelength range of 270 to 320 nm, we observed a predominant short-lived emission at 350 nm and a long-lived emission at 472 nm (Fig. 2e). This emission feature is characteristic of 4-PP, as there is no shift in emission wavelength when varying the excitation wavelength. Upon further shifting the excitation wavelength from 330 to 350 nm, the photoluminescence profiles exhibited corresponding redshifts to 370 and 400 nm, while the gated emission profiles showed redshifts to 488 and 500 nm (Supplementary Fig. 8), respectively. These emissions align well with the positions of SiO$_2$ defects, such as E'-defects, H-defects, and PRHT defects, albeit approximately 110 and 3.75 times more intense, suggesting efficient triplet-to-singlet state energy transfer from 4-PP to the defects. A comprehensive analysis of the excitation profiles for 4-PP, SiO$_2$ MPs, and 4-PP-doped SiO$_2$ MPs revealed that the spectral range from 240 to 260 nm, significantly deviating from the optimal excitation for 4-PP dopants, possibly contributes to the excitation of hybrid states of 4-PP and SiO$_2$ defects (Fig. 2f). This argument was supported by the observation of blueshifts in the afterglow of 4-PP-doped SiO$_2$ MPs when excitation at the short-wavelength region (Lower panel, Fig. 2b and Supplementary Fig. 8). The broadband nature of the excitation-dependent mapping spectra also unveiled the presence of multiple emission centers (Fig. 2g and Supplementary Fig. 9). The energy transfer from the 4-PP molecules to the defects was further supported by the observation of ultralong lifetime for the emission at 500 nm (Supplementary Fig. 10). Note that with increasing the excitation wavelengths, the excitation shifts from a combination of 4-PP and defects, to pure 4-PP and to another combination of 4-PP and defects, giving rise to a tendency of lifetime to initially increase and then decrease (Fig. 2h).
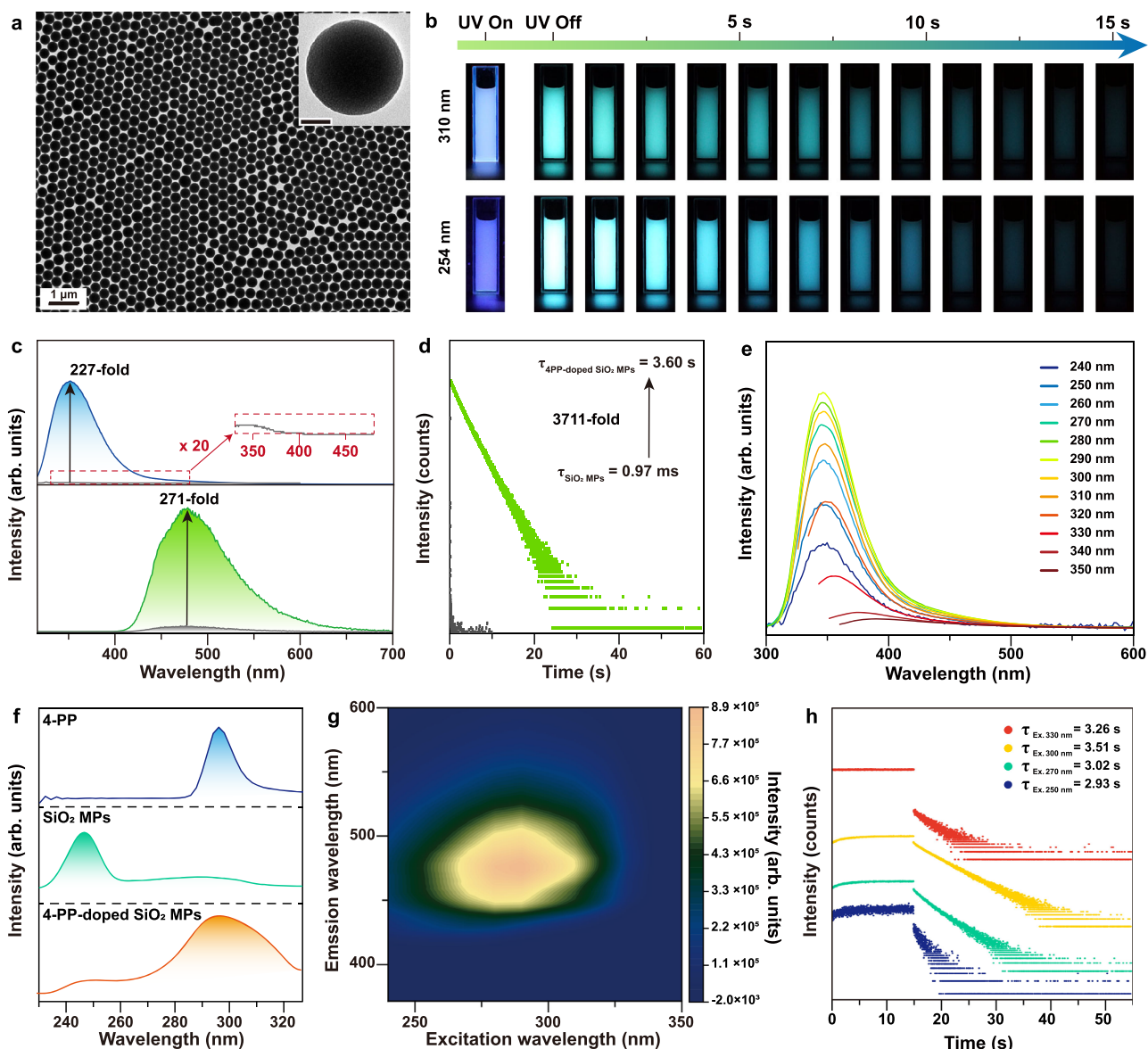
Fig. 2 | Characterization of 4-PP-doped SiO₂ MPs. a TEM image of the 4-PP-doped SiO₂ MPs. Inset: High-magnification TEM image displaying a single 4-PP-doped SiO₂ MP. Scale bar: 100 nm. **b** Luminescence photographs depicting an aqueous dispersion of 4-PP-doped SiO₂ MPs upon cessation of excitation wavelengths at 310 and 254 nm, respectively. **c** Comparative short- and long-lived emission of corresponding aqueous dispersions of 4-PP-doped SiO₂ MPs and SiO₂ MPs (10 mg mL^{-1}). Note that the delay time was fixed at 2 ms for obtaining the long-lived emission profiles. **d** Decay curves at 472 nm for SiO₂ MPs and 4-PP-doped SiO₂ MPs. **e** Luminescence spectra of the aqueous dispersion of 4-PP-doped SiO₂ MPs under

excitation at different wavelengths. **f** Comparison of the excitation spectra of corresponding short-lived emissions at 350 nm for a saturated aqueous solution of 4-PP molecules, aqueous dispersions of SiO₂ MPs, and 4-PP-doped SiO₂ MPs. **g** Two-dimensional excitation-dependent gated-emission of the aqueous dispersion of 4-PP-doped SiO₂ MPs. Note that the delay time was fixed at 2 ms for obtaining the long-lived emission profiles. **h** Decay curves of the cyan afterglow (472 nm) of the aqueous dispersion of 4-PP-doped SiO₂ MPs under different excitation wavelengths.

Note that excitation-dependent emission spectra were acquired at a temperature of 77 K, with the most prominent luminescent peak observed when the excitation was fixed at 290 nm. Under this excitation, the afterglow band was identified at 459 nm as a result of the direct excitation of the doped 4-PP molecules within the SiO₂ MPs. Note that the blueshift of the afterglow band from 472 to 459 nm is due to the suppression of energy dissipation resulting from limited matrix vibration at low temperatures (Upper panel, Fig. 3a). This effect allows the lifetime of the blue afterglow to increase to 5.05 s. Upon altering the excitation wavelength from 240 to 350 nm, a noticeable redshift of the afterglow band was observed, shifting from 450 to 500 nm due to the energy transfer from the triplet states of 4-PP molecules to the corresponding defects (Supplementary Fig. 11a, b). On a separate note,

in the excitation range from 250 to 290 nm, the lifetime for the afterglow was found to decrease with increasing the temperature (Fig. 3b). In addition, with a temperature increase from 293 to 673 K, the afterglow band at 472 nm gradually vanished, accompanied by the emergence of a new long-lived band at 375 nm (Lower panel, Fig. 3a), with a lifetime of 0.266 ms (Supplementary Fig. 12a). A corresponding fluorescence band was noted at the same wavelength under excitation at 290 nm, resulting from the radiative transition from the lowest singlet state (S₁) to the ground state (S₀) of 4-PP molecules via the reverse intersystem crossing (RISC) process, facilitated by thermal activation. Notably, the thermal treatment of the sample did not compromise the integrity of the doped 4-PP molecules, as evidenced by the re-observation of the same fluorescence and afterglow bands at
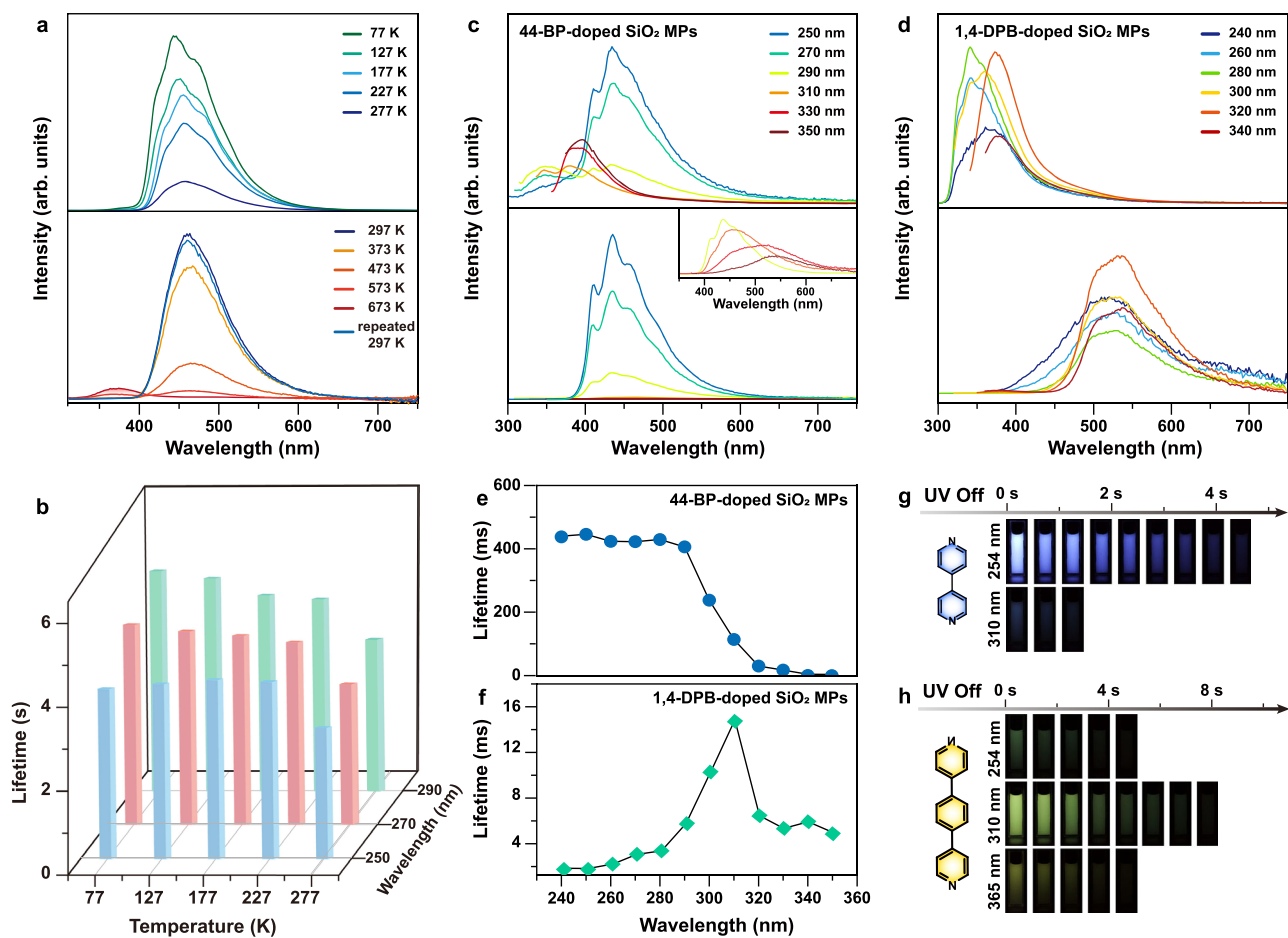
Fig. 3 | Photophysical characterization of 4-PP-, 4,4-BP-, and 1,4-DPB-doped SiO₂ MPs. a Long-lived emission profiles of 4-PP-doped SiO₂ MPs at varying temperatures. Note that the profile of 297 K listed below the profile of 673 K (Low panel) shows the afterglow profile obtained by repeating the measurement at 297 K after cooling down from 673 K. For obtaining the long-lived emissions, the delay time was fixed at 2 ms. **b** Cyan afterglow lifetime of 4-PP-doped SiO₂ MPs as a function of excitation wavelength and temperature. **c**, **d** Short- (upper panel) and long-lived (lower panel) emission profiles of 4,4-BP-doped SiO₂ MPs and 1,4-DPB-doped SiO₂ MPs under different excitation wavelengths. Note that the delay time was fixed at 2 ms for obtaining the long-lived emission profiles. **e**, **f** Blue afterglow lifetime of 4,4-BP-doped SiO₂ MPs and green afterglow lifetime of 1,4-DPB-doped SiO₂ MPs as a function of excitation wavelength. **g**, **h** Luminescence photographs illustrating aqueous dispersions of 4,4-BP-doped SiO₂ MPs and 1,4-DPB-doped SiO₂ MPs upon ceasing excitation at different wavelengths.

room temperature (Supplementary Fig. 12b, c). In addition, we observed the absence of thermally activated delayed fluorescence at high temperatures in hydrothermally treated SiO₂ MPs (Supplementary Fig. 12d).

Theoretical calculations suggest that the excitation is primarily associated with a π−π* transition. The heteroatom in 4-PP allows for the generation of an n→π*-type triplet state, thus facilitating the intersystem crossing through promoted spin-orbit coupling according to El-Sayed rules[43]. The spin-orbit coupling for the $S_1 \rightarrow T_1$ transition can be further improved due to the presence of a narrow energy gap between S_1 and T_1, enabling the efficient generation of afterglow for 4-PP (Supplementary Fig. 13 and Supplementary Data 1). These results suggest the ability of 4-PP dopants to generate long-lived phosphorescence when they are incorporated into a confined environment. For the defect-enriched SiO₂ matrix, the optical properties of the resulting 4-PP-doped SiO₂ MPs are an outcome of the interaction between the doped 4-PP molecules and the intrinsic defects within the SiO₂ MPs.

The optical properties of the resulting 4-PP-doped SiO₂ MPs were found to be notably influenced by hydrothermal reaction temperatures. As the reaction temperature increased from 100 to 180 °C, the interaction between the doped 4-PP and the matrix can be gradually improved by reduction of the density of −OH residual groups in the SiO₂ matrix by dehydration. The compression of 4-PP dopants by the matrix restricts their vibrational and rotational freedoms, possibly leading to a decreases in the energy gap between the highest occupied molecular orbital (HOMO) and the lowest unoccupied molecular orbital (LUMO), resulting in a pronounced redshift in the excitation profile. The argument is further supported by calculations showing that increasing the rigidity of the matrix, achieved by enhancing the content of Si(OSi)₄ in SiO₂ matrix, leads to a significant reduction in the energy gap by 0.78 eV (Supplementary Fig. 14 and Supplementary Data 1). The improved interaction between 4-PP and SiO₂ matrix resulted in a gradual increase in the afterglow intensity at 472 nm (Supplementary Fig. 15b), accompanied by an increase in afterglow lifetime from 3.19 to 3.60 s (Supplementary Fig. 15c). Notably, a further elevation of the reaction temperature to 200 °C led to a decline in both afterglow intensity and lifetime, possibly attributed to the formation of non-emissive defects that extract excitation energy from 4-PP dopants.

Formation of the high-quality SiO₂ matrix was confirmed through thermogravimetric spectroscopy, revealing that the mass loss of hydrothermally treated SiO₂ only reached 5.19% (Supplementary Fig. 16a). In stark contrast, the parent SiO₂ MPs exhibited a mass loss of up to 12.38% when the temperature was increased to 200 °C. These findings indicate that high-temperature hydrothermal reactions enable a more thorough dehydration condensation of silanol groups. Notably, the final mass loss for treated SiO₂ MPs and 4-PP-doped SiO₂ MPs remained essentially the same, suggesting no leakage of 4-PP molecules from the high-quality SiO₂ matrix during the

thermogravimetric measurement. This argument is further supported by ^{29}Si MAS NMR spectra (Supplementary Fig. 16b), revealing a significant enhancement in the portion of Si(OSi)$_4$ in 4-PP-doped SiO$_2$ when compared with the parent SiO$_2$ MPs. Furthermore, the decrease in the portion of Q$_3$ after UV irradiation also confirmed the photoresponsible defects generation. Our results showed that with enhancing the dosage of 4-PP in the precursor solution from 0.25 to 3.75 mg mL^{-1}, the doping level was gradually promoted from 0.095 to 0.136 wt% (Supplementary Fig. 17a). The results suggested that a saturated doping can be achieved when the dosage of 4-PP was enhanced to 2.5 mg mL^{-1}. The fluorescence and afterglow intensities were found to be gradually increased with enhancing the doping levels. In addition, the increase in the doping level of 4-PP in the SiO$_2$ MPs exhibited a negligible impact on the lifetime of the cyan afterglow (Supplementary Fig. 17b, c). We attributed this phenomenon to the fact that the nitrogen atom of 4-PP showed a strong coordination interaction with Si atoms[44], allowing for the distribution of 4-PP molecules in the SiO$_2$ matrix homogeneously. In addition, high-temperature pseudomorphic transformation likely facilitates the realization of 4-PP molecule doping other than 4-PP aggregates due to the presence of matrix channel confinement effects. Notably, the stabilization performance of the triplet states of the doped molecules by our strategy is comparable to that obtained by covalent doping, while retaining the monodisperse nature of the parent SiO$_2$ MPs[45–47].

Doping 4,4-BP and 1,4-DPB into SiO$_2$ MPs for afterglow tuning

To further elucidate the role of SiO$_2$ matrix in afterglow activation, we synthesized 4,4-BP-doped SiO$_2$ MPs and studied their optical properties. Our results showed similar morphology of the as-prepared 4,4-BP-doped SiO$_2$ MPs to 4-PP-doped SiO$_2$ MPs (Supplementary Figs. 18a, b and 19a). Upon excitation at the wavelength in the region of 250 to 290 nm, a strong blue emission was generated from an aqueous dispersion. And the blue emission was found to persist about 0.44 s, with a quantum yield of 9.49%. The blue emission was found to located at 435 nm, and the emission was defined as phosphorescence, because the emission intensity was enhanced 47.9-fold when the measured temperature dropped down to 77 K (Supplementary Fig. 20a–c). Note that the fluorescence of defects at 327 nm exhibited a remarkable 26.7-fold increase when excited within the 250 to 270 nm range. In addition, a redshift to 400 nm was observed when the excitation wavelength was shifted from 290 to 350 nm (Supplementary Fig. 20d–f). The observation of these emissions is likely due to the formation of different hybrid states of 4,4-BP and the intrinsic defects of SiO$_2$ matrix. Delay spectra showed that when shifting the excitation wavelength from 250 to 350 nm, the afterglow band was shifted gradually from 435 to 540 nm (Fig. 3c). This argument is supported by the fact that the afterglow emission at long wavelength is relatively weak, causing by a decreased energy transfer efficiency from the triplet states of 4,4-BP dopants to the defects due to the increase degree in the energy bandgaps. Another evidence is that the lifetime for the afterglow at 435 nm was found to be retained at 0.44 s when using excitation from 240 to 290 nm, and then to be decreased gradually to 3.09 ms when shifting the excitation wavelength to 350 nm (Fig. 3e).

Similarly, 1,4-DPB-doped SiO$_2$ MPs were further synthesized to elucidate the role of the intrinsic defects in the SiO$_2$ in influencing their optical properties (Fig. 3d, Supplementary Fig. 18c, d). When shifting the excitation wavelength from 240 to 340 nm, the short-lived emission bands is first blue-shifted from 356 to 340 nm, and then red-shifted to 372 nm. The strong band at 340 nm is likely attributed to the formation of molecule-defect hybrid states, while the emission band at 372 nm is primarily associated with the fluorescence of confined molecules. This fluorescence band of 1,4-DPB molecules aligns with the observations when the dopant is introduced into a PVA matrix (Supplementary Fig. 21a). Furthermore, we observed a shift in the

afterglow bands from 520 to 540 nm. Evidently, the former is caused by a synergy effect of 1,4-DPB-defect combinations, while the latter is contributed by the triplet emission of 1,4-DPB dopants. This finding is supported by the excitation-dependent afterglow lifetimes, revealing that excitation at 310 nm directly excites the doped 1,4-DPB dopants, generating an olive afterglow with a lifetime of 15.23 ms and a quantum yield of 15.67% (Fig. 3f). On a separate note, when excitation at short-wavelength (254 nm), the hybrid states of 1,4-DPB and ODC defect allows the luminescence to manifest in green, while excitation at long-wavelength (365 nm), afterglow color output allows to manifest in yellow benefitting from the hybrid states of 1,4-DPB and E' (or H) defect combinations (Fig. 3h).

Doping molecule emitters into other SiO$_2$ matrix

To validate the synthetic robustness, we conducted hydrothermal reactions involving 4-PP and SiO$_2$ gel at 180 °C for 10 h. Our study encompasses a one-pot large-scale synthesis, yielding 180.0 g of 4-PP-doped SiO$_2$ gel. The resultant materials displayed a long-lived afterglow at 482 nm, with a noteworthy lifetime of 3.44 s (Supplementary Fig. 22a–c). Note that in this thesis we extended the reaction time to 10 h to facilitate the pseudomorphic transformation of SiO$_2$ gel, thereby enhancing the incorporation of 4-PP molecules.

Photonic crystal fabrication application

The ability of our strategy to dope molecule emitters into SiO$_2$ MPs allows for the preparation of uniform multicolor building blocks for the creation of advanced photonic crystals[48–52]. These crystals have the capability to encode multi-dimensional information within their patterns by manifesting distinct color variations under different lighting conditions, showing potential as a spectroscopic platform for sensing applications (Fig. 4a)[53,54]. Initiating the photonic crystal fabrication involved employing a dip-coating strategy, resulting in the formation of multilayers of SiO$_2$ MPs that could be precisely patterned using a laser beam. The preservation of the highly ordered 3D structural features of the photonic crystal films was confirmed through SEM observations (Fig. 4b). As anticipated, the photonic crystals exhibited nearly identical reflectance spectra due to their consistent sizes, albeit with varying molecule dopants (Fig. 4c, Supplementary Fig. 23b, c). However, there was a marginal blueshift compared to the parent SiO$_2$ MPs as a result of their decrease in the average diameter. This characteristic allowed the patterned letters "I", "F", and "E" to undergo the same angle-dependent structural color transition—from orange to yellow and then to green—gradually altering with the observation angle ranging from 10° to 60°. The transition of the structure color outputs when increasing the observation angle can be explained by the following equation[55]:

$$\lambda_{max} = 1.633(d/m)(n_a^2 - \sin^2\theta)^{1/2} \tag{1}$$

where d represents the diameter of the MPs, m and θ represent the Bragg reflection order and the angle between the normal and incident light, respectively. The value of n_a is defined as the weighted sum of the refractive indices of the MP portion and the gap portion. The change in the angle between the normal and incident light leads to the corresponding change in the wavelength of the photons scattered.

Remarkably, upon irradiation at distinct wavelengths, particularly at 254 and 310 nm, the emission centers underwent notable alterations, leading to the generation of diverse afterglow scenarios. Specifically, with a fixed excitation at 310 nm, the predominant excitation of 4-PP and 1,4-DPB dopants resulted in the manifestation of a cyan "I" and a green "E" with extended persistence. Concurrently, hybrid states of 4,4-BP-defect were predominantly excited in the resultant SiO$_2$ MPs, yielding a shorter afterglow lifetime. In contrast, shifting the excitation wavelength to 254 nm led to the predominant excitation of molecule-defect combinations in 4-PP- and 1,4-DPB-doped SiO$_2$ MPs, while
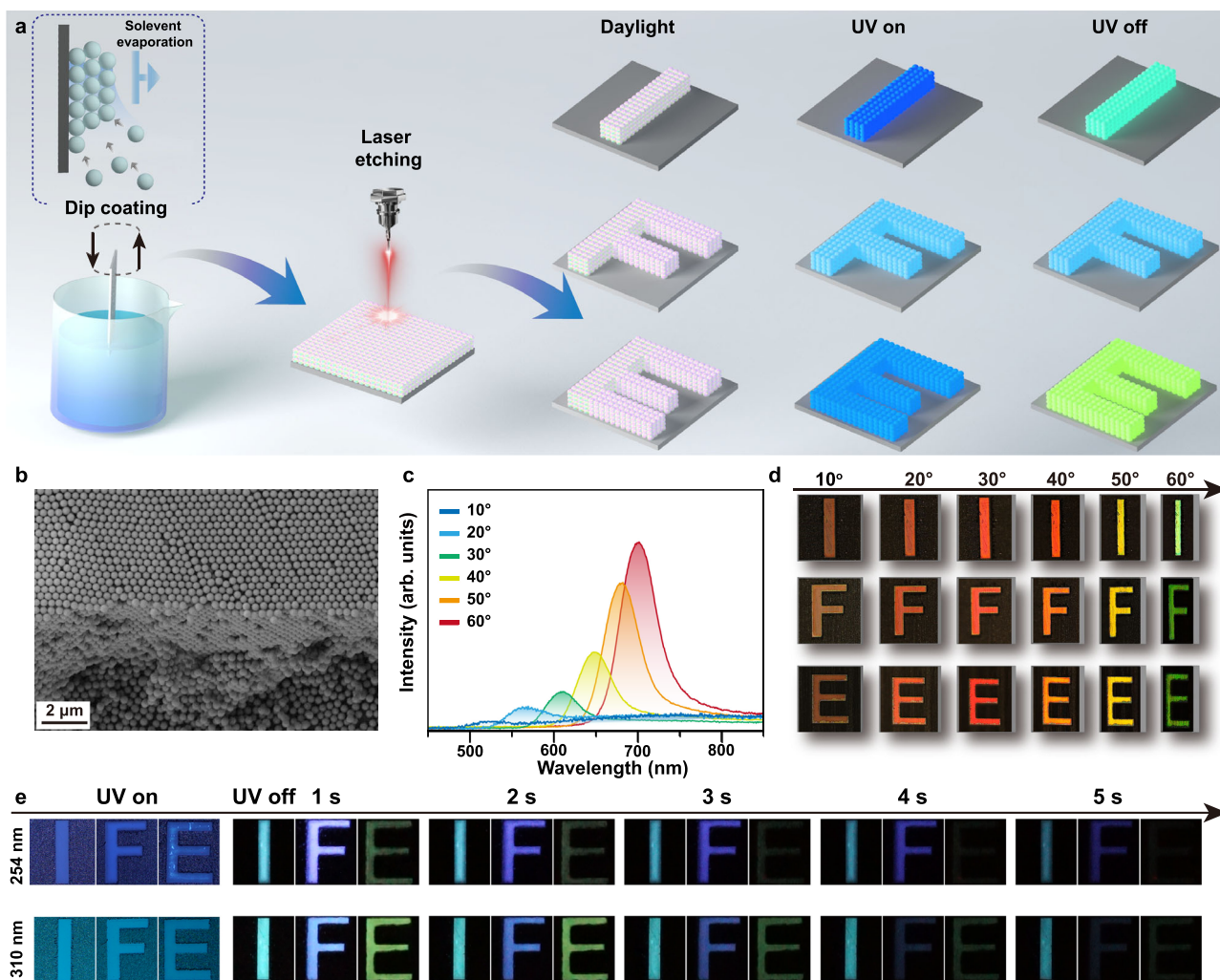
Fig. 4 | Application of molecule-doped SiO₂ MPs for the fabrication of photonic crystals. a Schematic illustration of the fabrication process involving 4-PP-, 4,4-BP-, and 1,4-DPB-doped SiO₂ MPs as building blocks. The process commences with a sequential dip-coating method, followed by a laser-assisted etching strategy to precisely sculpt the photonic crystal patterns into distinct "I", "F", and "E" shapes. The rationally designed patterns exhibit diverse optical characteristics in varying lighting conditions, including angle-dependent structural colors in natural daylight, luminescence color outputs upon UV irradiation, and distinct afterglow color emissions upon cessation of UV excitation. **b** SEM image showcasing a representative photonic crystal composed of 4-PP-doped SiO₂ MPs. **c** Reflectance spectra of photonic crystals formed with 4-PP-doped SiO₂ MPs at different incident angles. **d** Angle-dependent structural color outputs of the fabricated "I", "F", and "E"-shaped photonic crystals under natural daylight. **e** Luminescence images captured under UV excitation, along with time-dependent afterglow images of the pattern following the cessation of excitation. Notably, all images were captured at an observation angle of 0°.

4,4-BP dopants in SiO₂ were predominantly activated. This distinctive excitation profile gave rise to a prolonged afterglow time, particularly evident in the blue pattern "F". These findings underscore the adaptability of afterglow lifetimes in molecule-doped SiO₂ MPs, showcasing the ability to finely tune them by strategically exciting either molecule dopants or molecule-defect combinations.

Discussion

In summary, we elucidate the pivotal role of the SiO₂ matrix in activating the afterglow properties of small molecules. Beyond its role in providing a rigid framework with hydroxyl-enriched domains for stabilizing molecule dopants, the intrinsic defects inherent in the SiO₂ matrix facilitate the formation of dopant-defect combinations or the extraction of excitation energy through these dopants. This unique feature empowers the deliberate adjustment of afterglow lifetimes by selectively exciting the two distinct species. Furthermore, our innovative molecule doping strategy not only allows for the fabrication of SiO₂ MPs with multicolor afterglow properties, maintaining uniform diameters for the creation of photonic crystals, but also enables the

integration of structural and afterglow color tunability into a single platform. This capability holds promise for the creation of a versatile platform for information encoding, offering both structural and color-based tunability.

Methods

Preparation of monodisperse SiO₂ MPs

Monodisperse SiO₂ colloidal MPs were prepared by a modified Stöber method. In a typical experiment, 33 mL of DI water, 160 mL of ethanol, and 3.5 mL of ammonia solution (25–28%) were first mixed and heated to 60 °C. Next, 4.4 mL of TEOS was added dropwise to this solution, and the reaction was continued for 30 min under stirring to form the seed solution. A certain volume of the seed solution was then mixed with 10 mL of TEOS to form a clear mixture. Aqueous ammonia was added to the resultant mixture, and the mixture was allowed to react at room temperature for 10 h. The average diameter of the resulting SiO₂ colloidal MPs was estimated to be 359 nm when 0.2 mL of the volume of the seed solution was use. After the reaction, the product was centrifuged and washed several times with ethanol. SiO₂ suspension

(6 wt%) in ethanol was prepared by sonicating before photonic crystal fabrication.

Preparation of afterglow molecule-doped SiO$_2$ MPs

In brief, a mixture of molecule (5 mg) and SiO$_2$ MPs (50 mg, 4 mL water) was prepared which mixed at a 5-mL glass baker. The baker was transferred to a 20-mL polytetrafluoroethylene hydrothermal reactor and heated at 180 °C for 3 h. After cooling to room temperature, the resulting mixture was centrifuged at 10,142 × g for 5 min. The precipitate was purified through 3 cycles of alternate centrifugation and dispersion with DI water, and the final precipitate was dispersed in 3 mL of aqueous solution.

Fabrication of an ordered monolayer photonic structure

In a typical experiment, the substrates for building the photonic structures were washed with water before use. The dip-coating process was carried out at a temperature of 65 °C using a dip-coater from HeatMent (SYDC-100H DPI, SAN-YAN Instrument Co. Ltd., Shanghai). The pulling rate was set at 2 μm s^{-1}.

Characterization

Transmission electron microscopy was carried out on a HT7800 operating at an acceleration voltage of 100 kV. Scanning electron microscopy was performed using a Gemini SEM 300 (ZEISS). Photoluminescence emission profiles and decay curves were obtained using an FLS-1000 instrument from Edinburgh Instruments Ltd. Photoluminescence quantum yield (PLQY) measurements were performed with a C9920-02G instrument from Hamamatsu. The low-temperature spectroscopy tests are conducted using the Oxford OptistatDN liquid nitrogen cryostat, while the high-temperature spectroscopy tests are carried out by the Techcomp temperature controller. UV-Vis absorption spectra were taken on a Hitachi U-3900H ultraviolet-visible spectrophotometer. Dynamic light Scattering profiles were measured by Malvern Zeta sizer nano ZS. Electron paramagnetic resonance spectra was recorded on a Bruker EMXPLUS ESR spectrometer. Si solid-state NMR was performed by a nuclear magnetic resonance spectrometer with a super-conducting magnet (Bruker, Avance III HD 400 MHz). The photonic crystals were prepared using a dip-coating instrument (SYDC-100H, SAN-YAN Instrument Co. Ltd., Shanghai). The angle-dependent reflection spectra of the prepared photonic crystals were measured using an angular resolution spectral system, R1. A standard Al mirror (Ideaoptics STD-M) was used to serve as the ideal reflector reference.

Computational details

Using a Time-Dependent Density Functional Theory (TD-DFT) approach, the equilibrium configurations of the state and the excitation energies as well as the natural transition orbitals (NTOs) of the low-lying excited states, were performed at the rB3LYP/6-311 + G level. Based on the T$_1$-optimizted geometries, the spin-orbit coupling (SOC) matrix elements between singlet and triplet excited states were evaluated by Optimal Reciprocal Collision Avoidance (ORCA) program. The excitation energies for the HOMO and LUMO energy levels of 4-PP doped SiO$_2$ MPs were obtained by the DFT (density functional theory) method at B3LYP/6-31G(d) level. The geometries of 4-PP in the relaxed and rigidity structures of SiO$_2$ matrix have been optimized to lowest energy state for further theoretical calculations, and all the DFT calculations were performed using Gaussian 09 program.

Data availability

The data that support the findings of this study have been included in the main text and supplementary information. All other information can be obtained from the corresponding author upon request. Source data are provided with this paper.

References

1. Zwerver, A. M. J. et al. Qubits made by advanced semiconductor manufacturing. *Nat. Electron.* **5**, 184–190 (2022).
2. Zhu, K. et al. Hybrid 2D–CMOS microchips for memristive applications. *Nature* **618**, 57–62 (2023).
3. Lee, S. et al. Synthetic Rashba spin–orbit system using a silicon metal-oxide semiconductor. *Nat. Mater.* **20**, 1228–1232 (2021).
4. Deng, Y. C. et al. All-electrical switching of a topological non-collinear antiferromagnet at room temperature. *Natl. Sci. Rev.* **10**, 154 (2023).
5. Sun, C. et al. Efficient and stable white LEDs with silica-coated inorganic perovskite quantum dots. *Adv. Mater.* **28**, 10088–10094 (2016).
6. Sheen, M. et al. Highly efficient blue InGaN nanoscale light-emitting diodes. *Nature* **608**, 56–61 (2022).
7. Godefroo, S. et al. Classification and control of the origin of photoluminescence from Si nanocrystals. *Nat. Nanotech.* **3**, 174–178 (2008).
8. Lin, D. et al. A Silica-aerogel-reinforced composite polymer electrolyte with high ionic conductivity and high modulus. *Adv. Mater.* **30**, 1802661 (2018).
9. Fan, J. Y., Wu, X. L. & Chu, P. K. Low-dimensional SiC nanostructures: fabrication, luminescence, and electrical properties. *Prog. Mater. Sci.* **51**, 983–1031 (2006).
10. Tohmon, R. et al. 2.7-eV luminescence in as-manufactured high-purity silica glass. *Phys. Rev. Lett.* **62**, 1388 (1989).
11. Skuja, L. The origin of the intrinsic 1.9 eV luminescence band in glassy SiO$_2$. *J. Non-Cryst. Solids* **179**, 51–69 (1994).
12. Skuja, L. Optically active oxygen-deficiency-related centers in amorphous silicon dioxide. *J. Non-Cryst. Solids* **239**, 16–48 (1998).
13. Chen, H. et al. Germanium silicon oxide achieves multi-coloured ultra-long phosphorescence and delayed fluorescence at high temperature. *Nat. Commun.* **13**, 4438 (2022).
14. Paleari, A., Paleari, A., Meinardi, F., Brovelli, S. & Lorenzi, R. Competition between green self-trapped-exciton and red non-bridging-oxygen emissions in SiO$_2$ under interband excitation. *Commun. Phys.* **1**, 67 (2018).
15. Zhang, D. Y. et al. On-demand circularly polarized room-temperature phosphorescence in chiral nematic nanoporous silica films. *Adv. Opt. Mater.* **10**, 2102015 (2022).
16. Gelloz, B. & Koshida, N. Long-lived blue phosphorescence of oxidized and annealed nanocrystalline silicon. *Appl. Phys. Lett.* **94**, 201903 (2009).
17. Kong, D. Y. et al. Tunable photoluminescence in monodisperse silica spheres. *J. Colloid Interface Sci.* **325**, 279–284 (2010).
18. He, J. et al. Anchoring carbon nanodots onto nanosilica for phosphorescence enhancement and delayed fluorescence nascence in solid and liquid states. *Small* **16**, 2005228 (2020).
19. Liang, Y. C. et al. Phosphorescent carbon-nanodots-assisted Förster resonant energy transfer for achieving red afterglow in an aqueous solution. *ACS Nano* **15**, 16242–16254 (2021).
20. Sun, Y. et al. Ultralong lifetime and efficient room temperature phosphorescent carbon dots through multi-confinement structure design. *Nat. Commun.* **11**, 5591 (2020).
21. Xiao, F. et al. Guest-host doped strategy for constructing ultralong-lifetime near-infrared organic phosphorescence materials for bioimaging. *Nat. Commun.* **13**, 186 (2022).
22. Peng, H. et al. On-demand modulating afterglow color of water-soluble polymers through phosphorescence FRET for multicolor security printing. *Sci. Adv.* **8**, eabk2925 (2022).
23. Zhang, X. P. et al. Ultralong UV/mechano-excited room temperature phosphorescence from purely organic cluster excitons. *Nat. Commun.* **10**, 5161 (2019).
24. Huang, Q. Q. et al. Ultrastable and colorful afterglow from organic luminophores in amorphous nanocomposites: advanced

anti-counterfeiting and in vivo imaging application. *Nano Res.* **13**, 1035–1043 (2020).

25. Yang, X., Waterhouse, G. I. N., Lu, S. Y. & Yu, J. H. Recent advances in the design of afterglow materials: mechanisms, structural regulation strategies and applications. *Chem. Soc. Rev.* **52**, 8005–8058 (2023).

26. Chen, J. et al. Dynamic room temperature phosphorescence of silane-functionalized carbon dots confining within silica for anti-counterfeiting applications. *Small* **20**, 2306323 (2024).

27. Zhang, T. et al. Stable lignin-based afterglow materials with ultra-long phosphorescence lifetimes in solid-state and aqueous solution. *Green Chem.* **25**, 1406–1416 (2023).

28. Li, J. Y., Wang, B. L., Zhang, H. Y. & Yu, J. H. Carbon dots-in-matrix boosting intriguing luminescence properties and applications. *Small* **15**, 1805504 (2019).

29. Planas, O., Macia, N., Agut, M., Nonell, S. & Heyne, B. Distance-dependent plasmon-enhanced singlet oxygen production and emission for bacterial inactivation. *J. Am. Chem. Soc.* **138**, 2762–2768 (2016).

30. Grosch, H., Sárossy, Z., Egsgaard, H. & Fateev, A. UV absorption cross-sections of phenol and naphthalene at temperatures up to 500 °C. *J. Quant. Spectrosc. Radiat. Transf.* **156**, 17–23 (2015).

31. Cannas, M., Costa, S., Boscaino, R., Gelardi, F. M. & Post, U. V. irradiation annealing of E' centers in silica controlled by H_2 diffusion. *J. Non-Cryst. Solids* **337**, 9–14 (2004).

32. Wu, S. L., Xia, H. B., Xu, J. H., Sun, X. Q. & Liu, X. G. Manipulating luminescence of light emitters by photonic crystals. *Adv. Mater.* **30**, 1803362 (2018).

33. Shimakawa, K., Kolobov, A., Elliott, S. R. & Photoinduced, S. R. effects and metastability in amorphous semiconductors and insulators. *Adv. Phys.* **44**, 475–588 (1995).

34. Griscom, D. L. Defect structure of glasses. *J. Non-Cryst. Solids* **74**, 51–77 (1985).

35. Robertson, J. Intrinsic defects and hydroxyl groups in a-SiO_2. *J. Phys. C: Solid State Phys.* **17**, L221 (1984).

36. Zhao, Y. et al. Nonconventional aggregation-induced emission polysiloxanes: structures, characteristics, and applications. *Aggregate* **5**, e471 (2024).

37. He, T. et al. Ratiometric hypoxia detection by bright organic room temperature phosphorescence of uniformed silica nanoparticles in water. *Aggregate* **4**, e250 (2023).

38. Li, Q. et al. Induction of long-lived room temperature phosphorescence of carbon dots by water in hydrogen-bonded matrices. *Nat. Commun.* **9**, 734 (2018).

39. Li, D. et al. Completely aqueous processable stimulus responsive organic room temperature phosphorescence materials with tunable afterglow color. *Nat. Commun.* **13**, 347 (2022).

40. Xiong, S. D. et al. Achieving Tunable Organic afterglow and UV-irradiation-responsive ultralong room-temperature phosphorescence from pyridine-substituted triphenylamine derivatives. *Adv. Mater.* **35**, 2301874 (2023).

41. Gao, L. et al. Stepwise taming of triplet excitons via multiple confinements in intrinsic polymers for long-lived room-temperature phosphorescence. *Nat. Commun.* **14**, 7252 (2023).

42. Chen, X. et al. Pseudomorphic synthesis of monodisperse afterglow carbon dot-doped SiO_2 microparticles for photonic crystals. *Adv. Mater.* **35**, 2307198 (2023).

43. Ma, L. W., Liu, Y., Tian, W., Ma, H. & Switching, X. singlet exciton to triplet for efficient pure organic room-temperature phosphorescence by rational molecular design. *JACS Au* **3**, 1835–1842 (2023).

44. Rimola, A., Costa, D., Sodupe, M., Lambert, J. F. & Ugliengo, P. Silica surface features and their role in the adsorption of biomolecules: computational modeling and experiments. *Chem. Rev.* **113**, 4216–4313 (2013).

45. Ma, D. X. et al. Nylons with highly-bright and ultralong organic room-temperature phosphorescence. *Nat. Commun.* **15**, 4402 (2024).

46. Zhang, Y. et al. Ultraviolet irradiation-responsive dynamic ultralong organic phosphorescence in polymeric systems. *Nat. Commun.* **12**, 2297 (2021).

47. Bai, T., Zhang, Y., Wang, L., Yan, H. X. & Zhou, W. Construction of fluorescent hyperbranched polysiloxane-based clusterolumino-gens with enhanced quantum yield and efficient cellular lighting. *Aggregate* **4**, e267 (2023).

48. England, G. T. & Aizenberg, J. Emerging optical properties from the combination of simple optical effects. *Rep. Prog. Phys.* **81**, 016402 (2018).

49. Vukusic, P. & Sambles, J. Photonic structures in biology. *Nature* **424**, 852–855 (2003).

50. Boulenguez, J., Berthier, S. & Leroy, F. Multiple scaled disorder in the photonic structure of Morpho rhetenor butterfly. *Appl. Phys. A* **106**, 1005–1011 (2012).

51. Vukusic, P., Sambles, J. R. & Lawrence, C. R. Structurally assisted blackness in butterfly scales. *Proc. R. Soc. Lond. B.* **271**, S237–S239 (2004).

52. Sharma, V., Crne, M., Park, J. O. & Srinivasarao, M. Structural origin of circularly polarized iridescence in jeweled beetles. *Science* **325**, 449–451 (2009).

53. Cai, Z. Y. et al. From colloidal particles to photonic crystals: advances in self-assembly and their emerging applications. *Chem. Soc. Rev.* **50**, 5898–5951 (2021).

54. Liu, Y. F., Hou, X. Y., Song, Y. L. & Li, M. Z. Bioinspired reflective display based on photonic crystals. *Interdiscip. Mater.* **3**, 54–73 (2024).

55. Ge, J. P. & Yin, Y. D. Responsive photonic crystals. *Angew. Chem. Int. Ed.* **50**, 1492–1522 (2011).

Acknowledgements

Author contributions

X.L. and W.H. conceived and supervised the project. X.C. and M.C. designed the experiments and carried out the optical measurement experiments. W.X., Z.W., S.W., and Y.D.S. provided insightful discussion. X.C. and X.L. wrote the manuscript with input from other authors.

Competing interests

The authors declare no competing interests.

Additional information

Supplementary information The online version contains supplementary material available at https://doi.org/10.1038/s41467-024-51591-4.

Correspondence and requests for materials should be addressed to Xiaowang Liu or Wei Huang.

Peer review information *Nature Communications* thanks the anonymous reviewer(s) for their contribution to the peer review of this work. A peer review file is available.

Reprints and permissions information is available at http://www.nature.com/reprints